FRONTIERS OF PHYSICS

RESEARCH ARTICLE
Volume 21 / Issue 12 / 122201 / 2026

Differential interference metrology in crystal optics

Rong Wang[1], Qiang Yang[2], Xiaohui Ling[1,†], Hailu Luo[2,‡]

1 Laboratory for Spin-Orbit Photonics, College of Physics and Electronic Engineering, Hengyang Normal University, Hengyang 421002, China
2 Laboratory for Spin Photonics, School of Physics and Electronics, Hunan University, Changsha 410082, China
Corresponding authors. E-mail: †xhling@hynu.edu.cn, ‡hailuluo@hnu.edu.cn
Received January 22, 2026; accepted April 27, 2026

ABSTRACT

Conventional differential interference contrast (DIC) microscopy is inherently qualitative and lacks metrological capability, whereas high-precision techniques such as weak value amplification impose stringent experimental requirements. Here, we present a compact transmissive differential interferometric measurement system based on a birefringent crystal. By functioning as an interference element, the crystal enables quantitative differential interference measurements in both real space and momentum space. This approach avoids the dependence of weak value amplification on weak coupling and non-orthogonal state selection, while retaining and utilizing the inherent birefringent phase information of the crystal. We propose two modulation strategies and establish a unified theoretical model linking microscopic crystal parameters to macroscopic interferometric observations. Based on this model, the system can achieve an angular resolution on the order of 10^{-9} rad, which exceeds that of typical commercial polarimeters, and detects displacements as small as 0.35 nm, demonstrating nanometer-scale sensing capability. Owing to its compact design and tunable parameters, this system offers a compact quantitative approach for high-precision applications, including chiral sensing, nanometrology, and quantum material analysis.

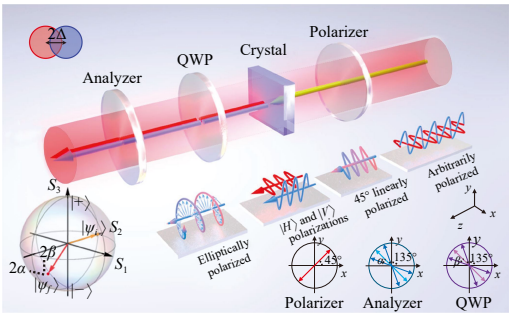

Keywords differential interference metrology, tunable birefringent crystal, quantitative measurement

1 Introduction

Conventional differential interference contrast (DIC) microscopy, introduced by Nomarski in 1955 [1, 2], is a label-free imaging technique that employs Wollaston or Nomarski prism. Its core principle involves real-space shear orthogonal polarization components to convert minute phase gradients in samples into visible intensity contrast. DIC has been widely adopted in biology [3–7], materials science [8–10], and surface topography inspection [11, 12], benefiting from its ability to reveal microscopic structures in transparent or weakly absorbing samples without staining. However, conventional DIC systems remain inherently non-quantitative due to fixed prisms, static polarization configurations, and the absence of an invertible signal model linking optical shear to physical phase gradients. In recent years, efforts to transform DIC microscopy into a quantitative imaging platform have advanced on multiple fronts [13], including the development of metasurface-based systems for edge detection and optical differentiation [14–18], the use of theoretical modeling and phase retrieval to enable quantitative DIC [19–22], optical spatial differentiation techniques [23, 24], and structured illumination for enhanced resolution without sacrificing quantitative accuracy [25]. While these innovations have significantly improved

https://doi.org/10.15302/frontphys.2026.122201

imaging quality, they primarily focus on visual enhancement rather than establishing a rigorous, linear mapping between image intensity and physical phase gradients required for precision metrology.

To address the escalating demands for precision measurement, weak value amplification (WVA) [26–30] has emerged as a prominent technological pathway. Recent advancements have further diversified the capabilities of WVA [31, 32]. Novel intensity-contrast-ratio pointers enable the decoupling of complex multi-parameter signals within a single measurement [33]. Furthermore, integrating WVA with surface plasmon resonance significantly enhances light-matter interaction for superior resolution [34], while adaptive schemes utilizing white light lasers demonstrate tunable sensitivity across a wide dynamic range [35]. When combined with the spin Hall effect of light [36–45], it can amplify nanoscale spin Hall effect shifts to the micrometer scale, enabling ultrasensitive detection [46–48]. Nevertheless, despite these recent sophistications, WVA-based metrology critically relies on strict weak coupling conditions and non-orthogonal pre- and post-selection states [49–51]. Deviations from these conditions can degrade its performance or even cause it to fail. Moreover, its output derived from complex weak values rather than direct physical displacements raises concerns about interpretability and metrological traceability. In contrast, birefringence-based measurement technology rooted in crystal optics provides a robust alternative [52–56]. These methods impose no stringent requirements on polarization orthogonality or coupling strength, while preserving the intrinsic symmetry information encoded in transverse optical responses. They also offer high stability and experimental simplicity. Nevertheless, despite their promise for precision metrology, a unified theoretical framework that bridges real-space shear operations with momentum-space optical responses in birefringent interferometry remains lacking. This gap not only limits the ability to fully harness the anisotropic properties of crystals but also constrains the overall precision, flexibility, and scope of application of the technique. This constraint hinders its development into a programmable, high-precision universal metrology platform.

This paper presents a compact transmissive differential interferometric measurement system that employs a birefringent crystal as a programmable interference element. The approach facilitates differential interference in both real and momentum space. It eliminates the stringent requirements associated with weak value amplification, such as weak coupling conditions and strict non-orthogonality selection, while retaining the intrinsic symmetry information of the crystal. Two modulation strategies are introduced, namely one based on independent rotation of the analyzer and the other involving coordinated adjustment of the quarter-wave plate (QWP) and the analyzer. These approaches can achieve a theoretical angular resolution of up to 10^{-9} rad and a displacement resolution of 0.35 nm, surpassing conventional polarimeters and confirming nanometer-scale sensing capability. Unlike conventional DIC microscopy, which prioritizes wide-field morphological imaging over absolute metrological precision, the proposed system is specifically engineered for trace-level quantification of minuscule physical parameters. The system is characterized by a compact architecture, tunable parameters, and straightforward integration. Its ultrahigh sensitivity and robustness make it particularly suitable for non-contact nanometrology of weakly anisotropic samples, chiral-sensitive biosensing such as protein binding detection, and real-time observation of dynamic phase transitions in quantum materials, offering a scalable pathway toward quantitative, crystal-based interferometric sensing beyond conventional imaging paradigms.

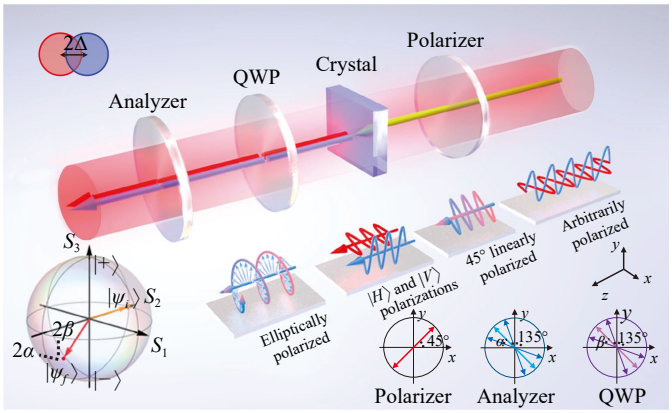

Fig. 1 Schematic illustration of the working principle of the crystal-based differential interferometric scheme for high-precision birefringence detection. Birefringence-sensitive interferometer operating in the horizontal ($|H\rangle$) and vertical ($|V\rangle$) linear polarization basis. The main optical components and their polarization transformations are shown. The lower-left inset illustrates the polarization trajectory on the Poincaré sphere, with $|\psi_i\rangle$ and $|\psi_f\rangle$ marking the pre- and post-selected states. The lower-right inset shows the coordinate system and angular settings of the polarization optics.

2 Theory and analysis

A propagation model is first established to investigate lateral differential interference effects in real space (r-space) and momentum space (k-space). As illustrated in Fig. 1, the coordinate systems in r-space and k-space are defined as (x, y, z) and (k_x, k_y, k_z), respectively. In the Cartesian coordinate system, the xy plane is parallel to the optical interface, and the z-axis is aligned with the central wave-vector component of the beam (i.e., the principal propagation direction). The unit vectors $\hat{\boldsymbol{e}}_x$ and $\hat{\boldsymbol{e}}_y$ define the horizontal and vertical directions in

this plane. After passing through a polarizer oriented at 45°, the light field of the Gaussian beam is expressed as

$$\boldsymbol{E}_1 = \frac{E_{\text{in}}}{\sqrt{2}}\,(\hat{\boldsymbol{e}}_x + \hat{\boldsymbol{e}}_y), \tag{1}$$

where $E_{\text{in}}(x,\,y) = \frac{1}{\sqrt{\pi}\,w_0}\exp\!\left(-\frac{x^2+y^2}{w_0^2}\right)$ represents the complex amplitude distribution of the beam. Here w_0 denotes the beam waist radius.

Two displacement scenarios arising from the interaction at the light–crystal interface are considered, namely a lateral shear δ in r-space (for a detailed derivation, see Appendix A) and a shear κ in k-space. In the interaction between light and crystal interfaces, two common displacements of a light beam are observed: r-space displacement δ and k-space shift κ. The r-space displacement reflects the transverse shift of the beam in position space, which arises from the interplay between the angular momentum of the beam, polarization state, and the interface. In contrast, the k-space displacement manifests as a shift in the angular spectrum of the beam, corresponding to a redistribution of photon momentum. These two displacements characterize the complete information of light–crystal interactions in the position domain and angular domain, respectively. By measuring both displacements, we can extract physical parameters of the interaction more comprehensively. The resulting light-field transformation is then given by

$$\boldsymbol{E}_2^{r\text{-space}}(x,y) \propto E_1(x+\delta,y)\,\hat{\boldsymbol{e}}_x + E_1(x-\delta,y)\,\hat{\boldsymbol{e}}_y, \tag{2}$$

$$\boldsymbol{E}_2^{k\text{-space}}(k_x,k_y) \propto E_1(k_x+\kappa,k_y)\,\hat{\boldsymbol{e}}_x + E_1(k_x-\kappa,k_y)\,\hat{\boldsymbol{e}}_y. \tag{3}$$

For the sake of clarity and convenience in subsequent analyses, the complex amplitudes of the horizontal and vertical components of $\boldsymbol{E}_2$ are denoted as h and v, respectively. Thus, the complex amplitude of the light field is expressed as $\boldsymbol{E}_2 = (h, v)^\top$. Subsequently, the beam is passed through a QWP, which introduces an optical path difference of $\lambda/4$ between the orthogonal polarization components, corresponding to a relative phase shift of $\pi/2$. Assuming that the fast axis of the QWP is rotated by an angle φ with respect to the x-axis, the corresponding Jones matrix is obtained by a similarity transformation based on the rotation matrix

$$\boldsymbol{R}(\varphi) = \begin{pmatrix} \cos\varphi & -\sin\varphi \\ \sin\varphi & \cos\varphi \end{pmatrix}. \tag{4}$$

Specifically, the Jones matrix of the rotated QWP is given by

$$\boldsymbol{J}_{\text{QWP}}(\varphi) = \boldsymbol{R}(\varphi)\,\boldsymbol{J}_{\text{QWP}}(0)\,\boldsymbol{R}(-\varphi),$$

where $\boldsymbol{J}_{\text{QWP}}(0)$ denotes the Jones matrix of the QWP when its fast axis is aligned with the x-axis. By combining Eqs. (1)–(4), the transformation of the light field is expressed as follows:

$$\boldsymbol{E}_3 = \boldsymbol{J}_{\text{QWP}}(\varphi)\boldsymbol{E}_2 = \frac{1}{\sqrt{2}}\begin{pmatrix} h - \mathrm{i}h\cos 2\varphi - \mathrm{i}v\sin 2\varphi \\ v + \mathrm{i}v\cos 2\varphi - \mathrm{i}h\sin 2\varphi \end{pmatrix}. \tag{5}$$

After transmission through an analyzer oriented at an angle θ relative to the x-axis, the electric field is projected onto the transmission axis of the analyzer. The resulting output field is given by

$$\begin{aligned} E_{\text{out}} = \frac{1}{\sqrt{2}}\big[&\cos\theta\,(h - \mathrm{i}h\cos 2\varphi - \mathrm{i}v\sin 2\varphi) \\ &+ \sin\theta\,(v + \mathrm{i}v\cos 2\varphi - \mathrm{i}h\sin 2\varphi)\big]. \end{aligned} \tag{6}$$

By substituting the rotation angles of the QWP and the analyzer into Eq. (6) with $\varphi = -\frac{\pi}{4} + \beta$ and $\theta = -\frac{\pi}{4} + \alpha + \beta$, and simplifying, a unified expression for the output field is obtained, which encompasses both r-space and k-space differential interference techniques, as follows:

$$E_{\text{out}}(p,\,q) = A\left[f_1(\alpha,\,\beta)\,E(p,\,q) + f_2(\alpha,\,\beta)\,\Delta\,\frac{\partial E(p,\,q)}{\partial p}\right], \tag{7}$$

where $f_1(\alpha,\,\beta) = \sin(\alpha+\beta) + \mathrm{i}\sin(\alpha-\beta)$ and $f_2(\alpha,\,\beta) = \cos(\alpha+\beta) - \mathrm{i}\cos(\alpha-\beta)$, with $p \in \{x,\,k_x\}$, $q \in \{y,\,k_y\}$, $\Delta \in \{\delta,\,\kappa\}$, and A a normalization constant. The optical field is expressed in a unified form as $E(p,\,q) = \exp\left[-C(p^2+q^2)\right]$, where the parameter C takes different forms depending on the physical space. In r-space, with $(p,\,q) = (x,\,y)$, C is given by $C = k/[2(r+\mathrm{i}z)]$, while in k-space, with $(p,\,q) = (k_x,\,k_y)$, it becomes $C = r/(2k)$. Here z denotes the propagation distance, and $r = \pi w_0^2/\lambda$ is the Rayleigh length, where λ is the wavelength.

Given the light field distribution of a transmitted beam, we quantify the amplified displacement arising from differential interference in r-space and k-space by the expectation value of the lateral displacement. To characterize this displacement directly in r-space, we employ Fourier duality to obtain the real-space field via the inverse Fourier transform $E(\boldsymbol{r}) = \mathcal{F}^{-1}\{E(\boldsymbol{k})\}$, where $\mathcal{F}^{-1}$ denotes the inverse Fourier transform. Based on this r-space representation, the expectation value of the lateral displacement is given by the centroid of the transverse intensity distribution:

$$\langle x\rangle = \frac{\iint x\,\left|E(x,\,y)\right|^2\,\mathrm{d}x\,\mathrm{d}y}{\iint \left|E(x,\,y)\right|^2\,\mathrm{d}x\,\mathrm{d}y}. \tag{8}$$

Substituting Eq. (7) into Eq. (8) yields the transverse displacement in real space induced by perturbations in r-

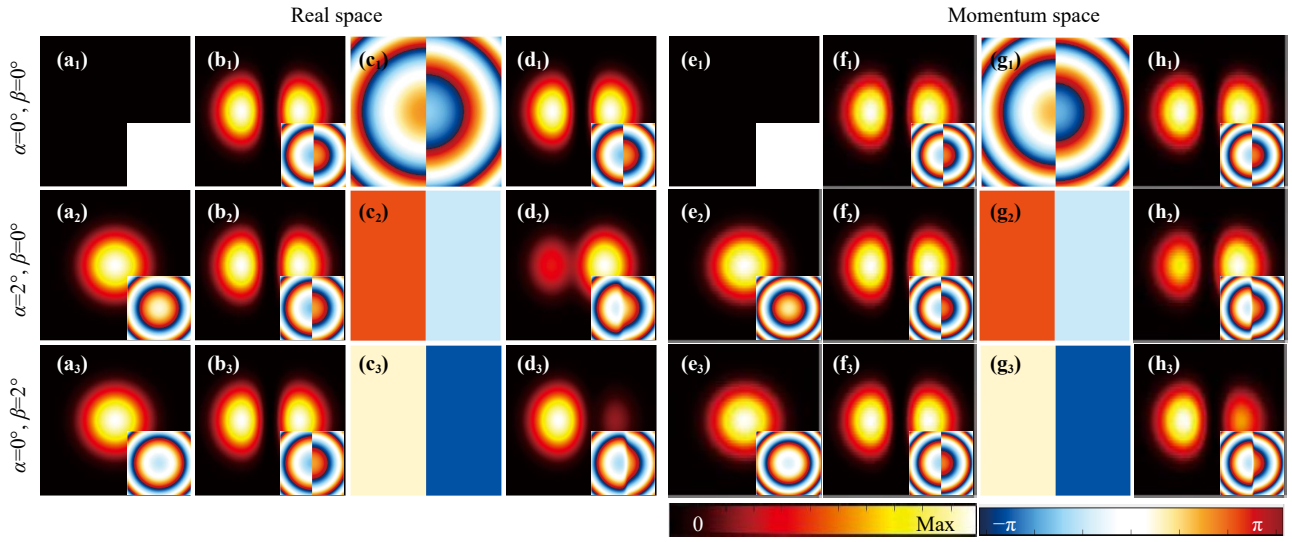

Fig. 2 Simulated beam interference patterns at $z = 400$ mm in r-space [panels $(\mathbf{a_i}-\mathbf{d_i})$, $\delta = 17.46$ μm] and k-space [panels $(\mathbf{e_i}-\mathbf{h_i})$, $\kappa = 6.52 \times 10^{-4}$ μm^{-1}]. (a_i, e_i) Intensity of the Gaussian field; (b_i, f_i) Intensity of its first-order x-derivative component; (c_i, g_i) Phase difference between the Gaussian field and its first-order derivative with respect to x; (d_i, h_i) Intensity of the resulting interference field. Insets show the corresponding phase distributions. Panels (a_i–d_i) share the (x, y) coordinate system; panels (e_i–h_i) share the (k_x, k_y) coordinate system. Index $i = 1$–3 corresponds to (α, β) angle pairs: (0°, 0°), (2°, 0°), and (0°, 2°).

space (δ) and k-space (κ), as follows:

$$\langle x\rangle_{\beta=0}^{r\text{-space}} = \frac{2z\delta\sin 2\alpha}{2r + k\delta^2 + \left(-2r + k\delta^2\right)\cos 2\alpha}, \tag{9}$$

$$\langle x\rangle_{\alpha=0}^{r\text{-space}} = -\frac{2r\delta\sin 2\beta}{2r + k\delta^2 + \left(-2r + k\delta^2\right)\cos 2\beta}, \tag{10}$$

$$\langle x\rangle_{\beta=0}^{k\text{-space}} = -\frac{2r\kappa\sin 2\alpha}{2k + r\kappa^2 - \left(2k - r\kappa^2\right)\cos 2\alpha}, \tag{11}$$

$$\langle x\rangle_{\alpha=0}^{k\text{-space}} = -\frac{2z\kappa\sin 2\beta}{2k + r\kappa^2 - \left(2k - r\kappa^2\right)\cos 2\beta}. \tag{12}$$

To improve readability, we simplify the above Eq. (9)–Eq. (12) as follows:

$$\langle x\rangle_{\beta=0}^{r\text{-space}} = \frac{z\delta\cot\alpha/r}{1 + \dfrac{\delta^2}{w_0^2}\cot^2\alpha}, \tag{13}$$

$$\langle x\rangle_{\alpha=0}^{r\text{-space}} = -\frac{\delta\cot\beta}{1 + \dfrac{\delta^2}{w_0^2}\cot^2\beta}, \tag{14}$$

$$\langle x\rangle_{\beta=0}^{k\text{-space}} = -\frac{\kappa w_0^2\cot\alpha/2r}{1 + \dfrac{1}{4}\kappa^2 w_0^2\cot^2\alpha}, \tag{15}$$

$$\langle x\rangle_{\alpha=0}^{k\text{-space}} = -\frac{z\kappa\cot\beta/2r}{1 + \dfrac{1}{4}\kappa^2 w_0^2\cot^2\beta}. \tag{16}$$

The above formula remains applicable under strong coupling conditions. In the modified weak measurement theory, the core criterion distinguishing strong from weak coupling relies on the relative magnitude of the transverse spin-splitting displacement δ versus the probe beam waist w_0, as well as the value of the post-selection angle α. According to the definition in Ref. [57], when the coupling is weak ($\delta \ll w_0$) and the post-selected state is not orthogonal to the pre-selected state, the modified theory should degenerate to the conventional weak measurement form. Specifically, for Eq. (13) and Eq. (14), the weak-coupling limit is governed by the dimensionless parameter $|\delta\cot\alpha|/w_0 \ll 1$, the nonlinear term $\delta^2\cot^2\alpha/w_0^2$ arising from strong coupling in the denominator becomes negligible. Consequently, Eq. (13) degenerates to $\langle x\rangle_{\beta=0}^{r\text{-space}} \approx z\delta\cot\alpha/r$, and Eq. (14) degenerates to $-\delta\cot\beta$, which aligns with the linear relationship of conventional theory where the amplified shift is proportional to $\delta\cot\alpha$.

For the more structurally complex formulas Eq. (15) and Eq. (16), the weak-coupling boundary condition is characterized by $\delta \ll w_0$ and $\sin^2\Delta$ not too small. Under these conditions, terms proportional to κ^2 in the denominator become negligible compared to terms proportional to $1/w_0^2$ or constant terms. Thus, the denominators of both Eq. (15) and Eq. (16) approximate to quantities independent of δ, simplifying the overall expressions to $-\kappa w_0^2\cot\alpha/2r$ and $-z\kappa w_0^2\cot\beta/2r$. This degenerative

behavior confirms the universality of these four modified formulas: they retain their full form in the strong-coupling regime to describe wave function distortion, while seamlessly transitioning to conventional weak measurement theory in the weak-coupling regime.

Next, we analyze the differential interference principle theoretically in both r-space [see Figs. 2(a_i)–(d_i)] and k-space [see Figs. 2(e_i)–(h_i)]. The physical mechanism can be interpreted by regarding the output field [see Eq. (7)] as resulting from interference between a Gaussian beam and its spatial derivatives. The balance between the contributions of the beam and its derivatives is governed by the parameters f_1 and f_2, which depend on the selected angles α and β. Adjusting these angles changes the relative weighting of the two contributions. On the Poincaré sphere, this corresponds to a change in the polarization state of the final beam (see lower-left inset of Fig. 1), and such variation directly affects the structure of the interference pattern, leading to distinct interference features.

First, we analyze the case of orthogonal pre- and post-selection states ($\alpha = 0, \beta = 0$) in r-space [Figs. 2(a_1)–(d_1)] and k-space [Figs. 2(e_1)–(h_1)]. In this configuration, destructive interference occurs for a phase difference of π, whereas constructive interference occurs for a phase difference of 0. According to the amplitude and phase values shown in the figures, the theory indicates complete destructive interference. The intensity distribution of the interference field exhibits a double-lobed profile symmetric about $p = 0$, as seen in Figs. 2(d_1) and (h_1).

Next, a post-selection angle is introduced by independently setting the rotation angles α and β. Specifically, when only the analyzer is rotated, which means that the QWP angle is fixed at $\beta = 0$ while $\alpha \neq 0$, the output field [see Eq. (7)] simplifies to $E_{\text{out}}(p, q) \propto (1 + \mathrm{i})\,[\sin\alpha\, E(p, q) - \mathrm{i}\cos\alpha\,\Delta\,\partial_p E(p, q)]$. This configuration corresponds to subfigures Figs. 2(a_i)–(h_i) with $i = 2$. The second term in this expression is purely imaginary and proportional to the transverse derivative $\partial_p E(p, q)$, corresponding to a $\pi/2$ phase shift relative to the original Gaussian beam. For quantitative phase analysis, the phase results from both the field and the derivative components are normalized to the interval $(-\pi, \pi)$. The resulting phase difference distribution shows an approximate phase jump of π at $p = 0$, indicating that the sensitive region for differential interference lies near this position. Under the current post selection angle condition, δ leads to an interference field with the central dark fringe disappearing and an asymmetric double peaked intensity profile, while κ produces an interference field that maintains a shifted central dark fringe and a pair of asymmetrically sized bright spots.

Further exploration is conducted on the differential interference effects obtained when the QWP and the analyzer are simultaneously rotated to an angle β. Under this condition, the governing equations for the system simplify to $E_{\text{out}}(p, q) \propto (1 - \mathrm{i})\sin\beta[E(p, q) + \cot\beta\,\Delta\,\partial_p E(p, q)]$. The second term in this expression is purely real and in phase with the original field $E(p, q)$, indicating sensitivity to the amplitude gradient rather than the phase gradient. The contribution of the gradient term is controlled by β. Under Case 2 conditions, Figs. 2(a_i)–(d_i) and Figs. 2(e_i)–(h_i) with $i = 3$ illustrate the intensities and phase distributions of the two types of interference field components in r-space and k-space, respectively. These include the Gaussian term, the partial differential term, and the final output interference field E_{out}. Comparison with the orthogonal-state case indicates that increasing β causes the interference field under δ spatial displacement to develop increasingly pronounced asymmetric lobes and a shift of the central dark fringe. In contrast, κ yields the opposite effect. The differential interference effect obtained by simultaneously rotating the quarter-wave plate and the analyzer in opposite directions by angles $-\alpha$ and $-\beta$, respectively, is presented in Appendix B. This configuration yields results that are symmetric with respect to those obtained with rotation angles $+\alpha$ and $+\beta$.

After thorough investigation of the differential interference effects induced by different post-selection angles, attention is further focused on the influence of the initial spatial displacement on the differential interference phenomenon. The differential interference phenomenon introduced by the two crystals is mainly affected by the magnitude of the initial displacement, with a smaller initial displacement resulting in more significant differential interference and higher corresponding measurement accuracy.

Finally, we analyze the displacement amplification effect arising from differential interference. The analysis indicates that, under the condition $\alpha \neq 0$ and $\beta = 0$, the amplified displacement depends on the propagation distance z and the real part $\mathrm{Re}[\Delta]$ of the initial lateral displacement Δ. Specifically, for an initial r-space shift, corresponding to $\mathrm{Re}[\Delta] \neq 0$ and $\mathrm{Im}[\Delta] = 0$, the amplified displacement varies with the transmission distance z, and its magnitude is positively correlated with $z \cdot \mathrm{Re}[\Delta]$. For an initial angular displacement ($\mathrm{Re}[\Delta] = 0$ and $\mathrm{Im}[\Delta] \neq 0$), the amplified displacement is negatively correlated with $r \cdot \mathrm{Im}[\Delta]$ and in this case it is independent of the transmission distance. When $\alpha = 0$ and $\beta \neq 0$, the dependence of the amplified displacement on displacement type and propagation distance is reversed. In this case, the amplified displacement is negatively correlated with both $z \cdot \mathrm{Im}[\Delta]$ and $r \cdot \mathrm{Re}[\Delta]$. Consequently, for an initial spatial displacement, the amplified displacement remains independent of the transmission distance, whereas an initial angular displacement leads to amplification that varies with z. Note that the specific interference pattern is also closely related to the beam waist radius. The waist radius determines the Rayleigh distance, which in turn governs the resulting differential interference phenomenon. In addition, the propagation distance

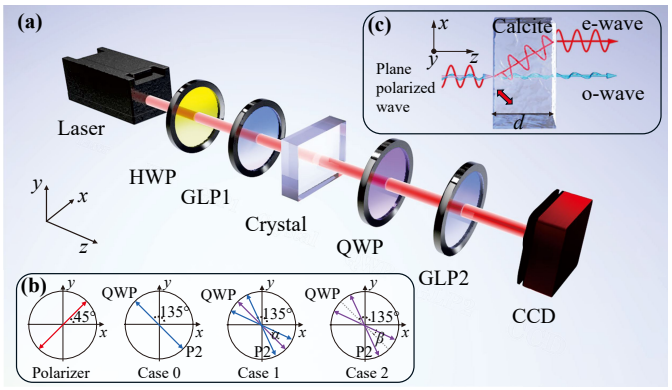

Fig. 3 Experimental setup for differential interference metrology. **(a)** Birefringence-sensitive vector differential interferometry setup. A 21 mW He–Ne laser emits a Gaussian beam ($w_0 = 0.35$ mm). A half-wave plate (HWP) adjusts the intensity. Glan–Laser polarizers GLP_1 and GLP_2, together with a quarter-wave plate (QWP), prepare the pre- and post-selected states. The output is recorded by a charge-coupled device (CCD) camera. **(b)** Coordinate system and pre-selected state. GLP_1 is oriented at $\pi/4$ relative to the x-axis. Three cases of post-selected state are considered: Case 0: GLP_2 and QWP are set at $-\pi/4$, orthogonal to GLP_1; Case 1: GLP_2 is at $-\pi/4+\alpha$, QWP at $-\pi/4$; Case 2: GLP_2 is at $-\pi/4+\alpha+\beta$, QWP at $-\pi/4+\beta$. **(c)** Optical path and polarization state evolution in the calcite crystal element. The red arrow indicates the direction of the optical axis.

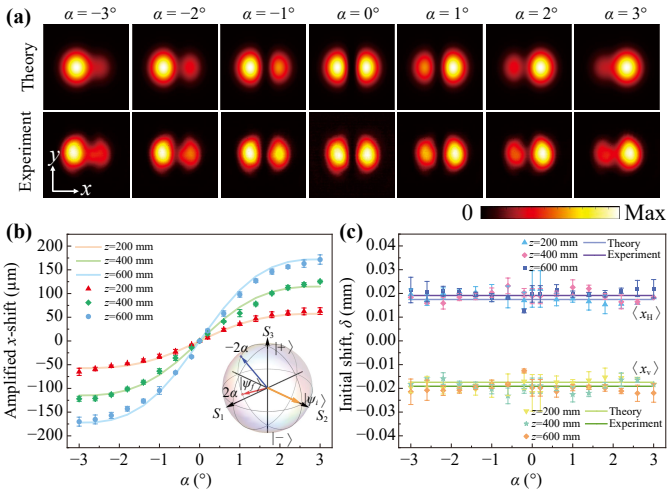

Fig. 4 Theoretical and experimental comparison of the differential interference results in r-space under Case 1 at three different propagation distances $z = 200$, 400, and 600 mm. **(a)** Intensity evolution. **(b)** Transverse amplified displacement results. Theoretical predictions are shown as solid lines, while experimental data are represented by solid points with error bars. The inset illustrates the trajectories of the initial and final selected states on the Poincaré sphere. **(c)** Initial displacement results. Experimental data simulation predictions and theoretical predictions are distinguished by solid lines of different colors. All data results were derived from statistical analysis of three replicate experiments.

modulates the interference effect, because the accumulated phase during propagation alters the relative phase between the interference components, thereby changing the diffraction pattern, as detailed in Appendix B.

3 Results and discussion

To validate the feasibility of the proposed approach, we employed calcite crystals and Nomarski prisms as test samples for differential interferometric measurements in r-space and k-space, respectively. The experimental setup is illustrated in Fig. 3. A Gaussian beam at wavelength $\lambda \approx 632.8$ nm is generated by a He–Ne laser. A half-wave plate (HWP), in conjunction with the first Glan–Laser polarizer (GLP_1), is used to prepare the preselected polarization state, while a QWP followed by the second Glan–Laser polarizer (GLP_2) enables precise post-selection of the output state. The resulting interference pattern is recorded by a CCD camera. Three post-selection configurations are defined in this study. Case 0 serves as the orthogonal reference condition where the QWP and GLP_2 are fixed at $-\pi/4$, ensuring the post-selected state is fully orthogonal to the pre-selected state. In Case 1, only GLP_2 is rotated to $-\pi/4+\alpha$ while the QWP is kept at $-\pi/4$. In Case 2, a coupled configuration is established by tuning the QWP to $-\pi/4+\beta$ and GLP_2 to $-\pi/4+\alpha+\beta$ to jointly control the post-selected polarization state.

First, a systematic investigation of the experimental results for the differential interference effect in r-space induced by a calcite crystal is conducted, and the results are compared rigorously with theoretical predictions. For Case 1, the real space interference field exhibits three distinctive features, that is, the gradual disappearance of the central dark fringe, a lateral displacement, and an asymmetric double-peak intensity distribution, as shown in Fig. 4(a). These phenomena result from incomplete destructive interference between the two polarization components, accompanied by evolution of the polarization state. Rotation of GLP_2 causes the initial linear polarization to evolve into an elliptical state, which means that the post-selection states on the Poincaré sphere are symmetric with respect to the S_2 axis along the same meridian, as illustrated in the inset of Fig. 4(b). Theoretical analysis predicts that the amplified displacement increases positively with the propagation distance z. This prediction is confirmed by experimental measurements at $z = 200$ mm, 400 mm, and 600 mm, where the measured displacement shows a strong positive correlation with z, as seen in Fig. 5(b). For Case 2, the r-space interference fringes undergo a global translation with pronounced asymmetry, producing one larger and one smaller spot, as shown in Fig. 5(a), and the beam centroid displacement remains independent of the propa-

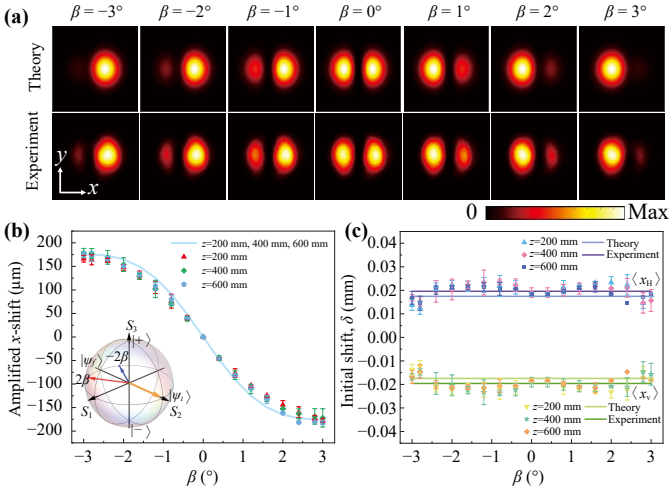

Fig. 5 Theoretical and experimental comparison of the differential interference results in r-space under Case 2 at three different propagation distances $z = 200$, 400, and 600 mm. **(a)** Intensity evolution. **(b)** Transverse amplified displacement results. Theoretical predictions are shown as solid lines, while experimental data are represented by solid points with error bars. The inset illustrates the trajectories of the initial and final selected states on the Poincaré sphere. **(c)** Initial displacement results. Experimental data simulation predictions and theoretical predictions are distinguished by solid lines of different colors.

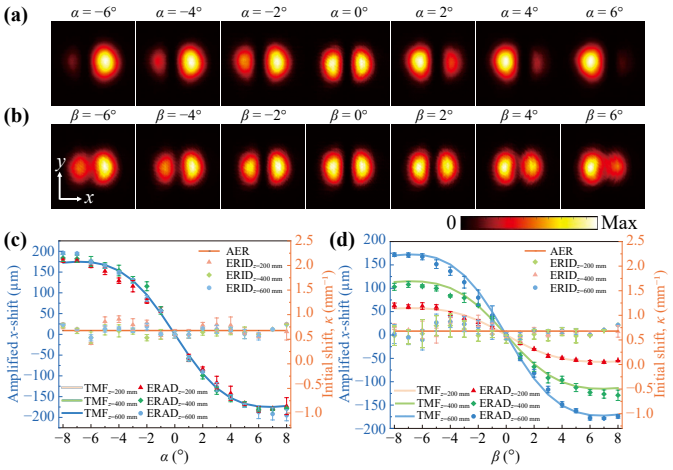

Fig. 6 Theoretical and experimental comparison of the differential interference results in k-space at three different propagation distances $z = 200$, 400, and 600 mm. **(a)** Intensity evolution under Case 1. **(b)** Intensity evolution under Case 2. **(c, d)** Measured transverse displacement at a selected angle together with crystal parameter measurement results for Case 1 and Case 2, incorporating the theoretical model fitting (TMF), experimental results of amplified displacement (ERAD), experimental results of initial displacement (ERID), and the average of experimental results (AER). Subscripts indicate the corresponding transmission distances of $z = 200, 400$, and 600 mm, respectively. Theoretical predictions are shown as solid lines, while experimental data are represented by solid points with error bars.

gation distance. Experimental results are consistent with the prediction of Eq. (10), as shown in Fig. 5(b). In this case, the post-selection states correspond to motion along the equator of the Poincaré sphere, as illustrated in the inset of Fig. 5(b).

Subsequently, a Nomarski prism is used as a test case, and differential interference phenomena caused by displacement perturbations in k-space are observed during the experiment. Based on Fourier duality, a local displacement in k-space corresponds to a linear phase modulation in r-space, while a phase modulation in k-space induces a tilt or shift in the overall interference fringes in r-space. Based on the analysis in section II, we can know that when the initial displacement manifests as a momentum-space translation, the resulting interference pattern exhibits an asymmetric double-peak distribution, translation of the dark fringe, and displacement of the beam centroid for Case 1. All these effects become progressively more pronounced with increasing rotation angle. This prediction is clearly verified in Fig. 6(a). For Case 2, as the rotation angle increases, the central dark fringe gradually vanishes, accompanied by a transverse shift of the beam centroid [see Fig. 6(b)]. Analysis of the measured displacement values [see Figs. 6(c) and (d)] further supports this finding. This not only validates the experimental approach but also reinforces the intrinsic unity of interference effects within this dual space.

Based on the theoretical framework of the quantitative relationship between the amplified and initial displacements established in Section 2 and the experimentally measured amplified displacement data, an application is subsequently developed. This application focuses on the determination of the intrinsic parameters of the crystal. When the propagation distance z is much greater than the Rayleigh length r, the system operates in the far-field regime, where the beam exhibits a significant lateral shift. Independent inversions are performed for each propagation distance, and the average of the measured results is taken to improve the reliability of the data. The horizontal and vertical polarization components are assumed to undergo equal lateral displacement. In Case 1, the mean values of the initial displacement obtained from theoretical prediction and experimental inversion are 17.46 μm and 19.13 μm, respectively [see Fig. 4(c)]. In Case 2, the corresponding values are 17.46 μm and 19.58 μm [see Fig. 5(c)]. The high degree of agreement between the theoretical and experimental values demonstrates that the proposed scheme can accurately characterize the r-space displacement induced by a birefringent crystal.

Next, we calculate the initial displacement introduced by the Nomarski prism. As indicated by Eqs. (11) and (12), the amplified lateral displacement is independent of the propagation distance z in Case 1, whereas it

exhibits a z-dependent relationship in Case 2. By fitting the experimental results for both cases, the initial displacement values are obtained. The k-space analysis presented in Section 2 shows that the intrinsic lateral momentum shift κ induced by the crystal birefringence has units of μm^{-1}. The experimentally determined values are $\kappa_{exp} = 6.77 \times 10^{-4}$ μm^{-1} for Case 1 and 6.79×10^{-4} μm^{-1} for Case 2 [see Figs. 6(c) and (d)], respectively. The experimental results are also in good agreement with the theoretical fit. The slight overestimation compared to the theoretical predictions is attributed to minor optical alignment issues or environmental disturbances.

We investigate the sensitivity and resolution of the system using a tunable birefringent crystal as an example. As shown in Figs. 4–6, the amplified displacement exhibits a linear response in the vicinity of zero post-selection angle, indicating high sensitivity to small variations in the original displacement δ. Consequently, the analysis is focused on this linear regime. We define the system sensitivity parameter as the linear response coefficient of ϑ in the limit $\vartheta \to 0$, namely

$$K = \left. \frac{\partial \langle x \rangle}{\partial \vartheta} \right|_{\vartheta = 0}, \tag{17}$$

where $\vartheta \in \{\alpha, \beta\}$ denotes either post-selection angle. For sufficiently small ϑ, the displacement is approximated by the linear relation $\langle x \rangle \approx K\vartheta$, with K having units $\mu m \cdot rad^{-1}$. Within the linear response framework, the response coefficients for the two tuning modes are derived as $K_1 \approx \frac{2z}{k\delta}$, $K_2 \approx -\frac{2r}{k\delta}$. The parameter δ is determined by intrinsic crystal properties such as thickness d, refractive index ratio n_o/n_e, and optical axis orientation ν. Under the small-angle approximation, K_1 and K_2 vary inversely with δ.

Figure 7 presents the influence of crystal parameters on sensitivity and displacement amplification, based on the theoretical model from Section 2. As illustrated in Fig. 7(a), the sensitivities K_1 and K_2 for quartz ($n_o = 1.5438$, $n_e = 1.535$) with the optical axis fixed at $\nu = 0.1°$ decrease with increasing crystal thickness d, since a larger d leads to a larger δ, which in turn reduces sensitivity. Consequently, the highest sensitivities are achieved at the minimum practical thickness $d = 0.1$ mm, yielding $K_1 \approx -2 \times 10^7$ $\mu m \cdot rad^{-1}$ and $K_2 \approx 1.22 \times 10^8$ $\mu m \cdot rad^{-1}$. In contrast, Fig. 7(b) shows that, at a fixed thickness $d = 0.1$ mm, the sensitivity varies with the refractive index ratio n_o/n_e. As $n_o/n_e \to 1$, the parameter $\delta \to 0$ and the sensitivity diverges, thereby enabling extreme amplification in the vicinity of the isotropic limit. However, this divergence ceases to occur for truly isotropic crystals, for which $n_o = n_e$ eliminates birefringence and thus removes the underlying mechanism for displacement amplification. Furthermore, Figs. 7(c) and (d) depict the amplified displacement for Case 1 and Case 2 at a crystal thickness

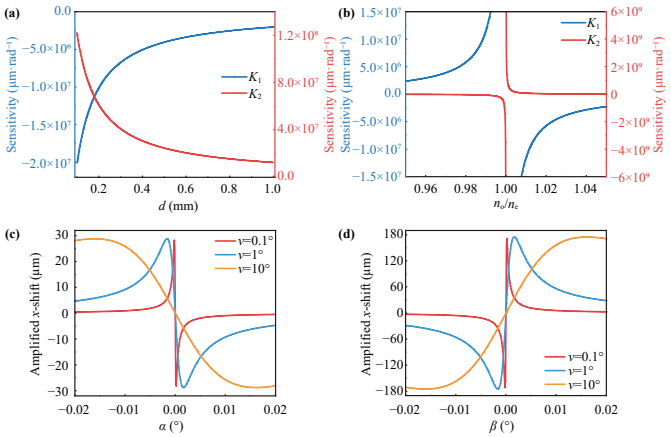

Fig. 7 Effects of crystal parameters on sensitivity and displacement amplification. For all cases, $z = 10$ cm. **(a)** Sensitivity (K_1, K_2) vs. thickness h for quartz ($n_o = 1.5438$, $n_e = 1.535$). **(b)** Sensitivity vs. refractive index ratio n_o/n_e, with $d = 0.1$ mm. **(c, d)** Amplified displacement for Case 1 and Case 2 at $d = 0.1$ mm and $\nu = 0.1°$, $1°$, $10°$.

of $d = 0.1$ mm and for optical axis orientations $\nu = 0.1°$, $1°$, $10°$. These results indicate that a smaller ν produces a steeper linear slope, leading to larger amplification and higher sensitivity. Across all tested configurations, Case 2, which is realized through polarization cooperative control, achieves a significantly higher displacement amplification factor than Case 1.

The displacement amplification factor is defined as

$$M = \left| \frac{\langle x \rangle}{\delta} \right|. \tag{18}$$

Based on Eqs. (9) and (10) in Section 2 and assuming an extremely small initial displacement, the amplification factors for the two modulation strategies are given by $M_1 \approx \left| \frac{z}{r} \cot \alpha \right|$, $M_2 \approx |-\cot \beta|$, For fixed propagation distance z and Rayleigh length r, M_1 is inversely proportional to $\tan \alpha$ (approximately to α in the small-angle limit) and directly proportional to z, while M_2 is determined solely by β and is inversely proportional to $\tan \beta$ (approximately to β for small angles).

Using the parameter values specified in the model, the minimum detectable displacement is taken as $\langle x \rangle_{min} = 1$ μm, the minimum effective rotation angle is $0.02°$ for both α and β, propagation distance $z = 10$ cm. Substitution into the theoretical expressions yields maximum amplification factors $M_{1,max} \approx 471$ and $M_{2,max} \approx 2865$. The minimum measurable original displacement follows from $\delta_{min} = \frac{\langle x \rangle_{min}}{M}$. With $\langle x \rangle_{min} = 1$ μm, the theoretical results give $\delta_{1,min} \approx 2.12$ nm for Case 1 and $\delta_{2,min} \approx 0.35$ nm for Case 2.

From Eq. (17), the measurement resolution for the post-selection angle, denoted S, is defined as the smallest angular change corresponding to a detectable displacement of $\langle x \rangle_{min}$. It is given by $S = \left| \frac{\langle x \rangle_{min}}{K} \right| = \left| \frac{1}{K} \right|$, with units rad.

Under optimal conditions ($d = 0.1\,\text{mm}$, $\nu = 0.1^\circ$), the theoretical results give $S \approx 5 \times 10^{-8}\,\text{rad}$ for Case 1 and $S \approx 8.2 \times 10^{-9}\,\text{rad}$ for Case 2, representing a four-order-of-magnitude improvement over conventional polarimeters [58]. The compact, alignment-free transmission geometry renders the system well suited for real-time monitoring of dynamic chiral processes in liquid samples, as supported by the derived performance estimates.

The proposed transmission-based differential interferometric amplification architecture is directly applicable to the characterization of chiral materials. In contrast to the reflective configuration of Wang *et al.* [59], which employs spin-dependent splitting at an air–prism interface and exhibits complex alignment requirements together with limited mechanical stability, the present approach eliminates the requirement for precision angular alignment. This yields a more robust and compact configuration, which is inherently compatible with liquid cells or microfluidic chips, thereby significantly reducing susceptibility to environmental disturbances and sample positioning errors. A central advantage of the approach lies in the integration of differential interferometry with arbitrary elliptical post-selection. This strategy not only enhances measurement precision but also overcomes limitations inherent in conventional linear post-selection, enabling full reconstruction of the polarization response. Consequently, the detectable parameter space encompasses not only optical activity but also film thickness, refractive index, surface microstructure, and optical anisotropy. The transmission geometry confers superior signal-to-noise performance in the strong-coupling regime, enhancing metrological robustness. Thus, through comprehensive polarimetric analysis and flexible access to multiple parameters, the method affords exceptional sensitivity for chiral sensing and remains readily transferable to other high-precision applications, such as characterization of surface topography and microstructure. This versatility establishes a robust foundation for a versatile, integrated platform for precision optical metrology.

4 Conclusion

In summary, a compact transmissive differential interferometry system is realized by use of birefringent crystals as programmable interference elements, enabling differential interference measurement in r-space and k-space. While avoidance of the stringent requirements of weak value amplification for weak coupling and non-orthogonal pre- and post-selected states is achieved, preservation of birefringent phase information of the crystals is maintained. A unified theoretical mechanism, combining two modulation strategies, is established to describe the amplification process, resolving ambiguities in the strong-coupling regime and linking microscopic crystal parameters with macroscopic interferometric observations. Transformation of differential interference from a qualitative tool into a high-precision metrology method is demonstrated, with angular resolution reaching $10^{-9}\,\text{rad}$. The system can detect a minimum initial displacement of 0.35 nm, demonstrating nanometer-level displacement detection capability. The system features compactness, tunability, and facile integration, opening new possibilities for non-contact nanometrology, in-situ photonic device diagnostics, chiral-sensitive biosensing, real-time monitoring of dynamic phase transitions, and symmetry analysis of quantum materials. This advances crystal-based interferometry beyond conventional imaging paradigms toward quantitative high-resolution sensing.

Declarations The authors declare that they have no competing interests and there are no conflicts.

Acknowledgements This work was supported by the National Natural Science Foundation of China (Grant No. 12574322).

Appendix A: Displacement calculation induced by tilted optical axis in calcite crystals

The optical properties of crystals and their operational mechanisms within the system are derived theoretically in this section. The crystal structure is shown in Fig. 3(c). In the electromagnetic theory developed by Maxwell, the polarization state of a medium is characterized by permittivity ε. For anisotropic crystals, the anisotropy of polarization gives rise to a linear relation between electric displacement $\boldsymbol{D}$ and electric field $\boldsymbol{E}$, which is expressed as $\boldsymbol{D} = [\varepsilon]\boldsymbol{E}$, where $[\varepsilon]$ is referred to as the dielectric tensor. In a Cartesian coordinate system, the dielectric tensor is represented in a diagonal form as $\text{diag}(\varepsilon_x, \varepsilon_y, \varepsilon_z)$. In this representation, the three mutually perpendicular directions x, y, and z are taken as the principal axes of the crystal, and ε_x, ε_y, ε_z are designated as the principal permittivities. Only uniaxial crystals are considered, for which $\varepsilon_x = \varepsilon_y \neq \varepsilon_z$. By employing the relation between refractive index and relative permittivity, $n_i = \sqrt{\varepsilon_i}$ for $i = x, y, z$, it is obtained that $n_x = n_y = n_\text{o}$ and $n_z = n_\text{e}$, where n_o and n_e denote the ordinary and extraordinary refractive indices, respectively.

For simplicity, the incident wave normal $\boldsymbol{k}_0$ is assumed to lie in the xz-plane. Its components are given by $k_{0x} = \sin\nu$, $k_{0y} = 0$, $k_{0z} = \cos\nu$, where ν is defined as the angle between $\boldsymbol{k}_0$ and the optical axis aligned with the z-axis. In this case, k_{0x}, k_{0y}, k_{0z} are interpreted as the components of the wavevector in vacuum normalized by k_0, with $k_0 = \omega/c$. These expressions are substituted into the Fresnel equation [60]

$$\frac{k_{0x}^2}{\frac{1}{n^2}-\frac{1}{\varepsilon_{rx}}}+\frac{k_{0y}^2}{\frac{1}{n^2}-\frac{1}{\varepsilon_{ry}}}+\frac{k_{0z}^2}{\frac{1}{n^2}-\frac{1}{\varepsilon_{rz}}}=0, \tag{A1}$$

where ε_{ri} with $i=x,y,z$ represents the relative permittivity along the corresponding principal axis. By setting $\varepsilon_{rx}=\varepsilon_{ry}=n_o^2$ and $\varepsilon_{rz}=n_e^2$, two distinct real solutions for n^2 are obtained:

$$\begin{cases} n_1^2=n_o^2, \\ n_2^2=\dfrac{n_o^2 n_e^2}{n_o^2\sin^2\nu+n_e^2\cos^2\nu}. \end{cases} \tag{A2}$$

The first solution $n_1=n_o$ is associated with the ordinary wave, whose refractive index remains independent of the direction of $\boldsymbol{k}_0$ relative to the optical axis. The second solution n_2 corresponds to the extraordinary wave, for which the refractive index is dependent on ν.

It is shown that a uniaxial crystal supports two eigenwaves for a given wave normal direction. One corresponds to the ordinary wave, for which the refractive index $n_1=n_o$ remains constant irrespective of the propagation direction. The other corresponds to the extraordinary wave, for which the refractive index n_2 varies with the angle ν.

The vibration directions of the ordinary (o) and extraordinary (e) waves are determined in the following. From the equations of Maxwell and the constitutive relations, the electric displacement vector is given by $\boldsymbol{D}=\varepsilon_0\boldsymbol{\varepsilon}_r\cdot\boldsymbol{E}=-\varepsilon_0 n^2\,\boldsymbol{k}_0\times(\boldsymbol{k}_0\times\boldsymbol{E})$, where ε_0 and μ_0 are the vacuum permittivity and permeability, respectively. Since $\boldsymbol{D}$ is perpendicular to $\boldsymbol{k}_0$, it follows that $\boldsymbol{D}\cdot\boldsymbol{k}_0=0$. By expressing this condition in the principal-axis frame and using $\varepsilon_i=\varepsilon_0\varepsilon_{ri}$ $(i=x,y,z)$, the following system is obtained after simplification:

$$\begin{cases} (n_o^2-n^2\cos^2\nu)E_x+n^2\sin\nu\cos\nu\,E_z=0, \\ (n_o^2-n^2)E_y=0, \\ n^2\sin\nu\cos\nu\,E_x+(n_e^2-n^2\sin^2\nu)E_z=0. \end{cases} \tag{A3}$$

For the o-wave, $n=n_o$ is substituted. The second equation permits a nonzero E_y, whereas the first and third equations lead to $E_x=E_z=0$. Consequently, $\boldsymbol{D}$ possesses only a y-component, $D_y=\varepsilon_0\varepsilon_{ry}E_y\neq0$, and is found to be parallel to $\boldsymbol{E}$. Both vectors are perpendicular to the xz-plane, which contains the wave normal $\boldsymbol{k}_0$ and the optical axis.

For the e-wave, $n=n_2$ is set. In this case, the second equation forces $E_y=0$, so $D_y=\varepsilon_0\varepsilon_{ry}E_y=0$, and the displacement vector is confined to the xz-plane. Solution of the first and third equations yields the ratio $\frac{D_z}{D_x}=\frac{\varepsilon_{rz}E_z}{\varepsilon_{rx}E_x}=-\frac{\sin\nu}{\cos\nu}$. Thus, $\boldsymbol{D}$ and $\boldsymbol{E}$ are generally not collinear. Moreover, the direction of energy flow, represented by the Poynting vector $\boldsymbol{S}\propto\boldsymbol{E}\times\boldsymbol{H}$, is different from the wave normal $\boldsymbol{k}_0$, leading to spatial walk-off of the e-ray.

By combining Eqs. (A1)–(A3), the walk-off angle α is obtained, defined as the angle between the wave normal and the ray direction,

$$\tan\alpha=\tan(\nu-\nu')=\left(n_e^2-n_o^2\right)\frac{\tan\nu}{n_e^2+n_o^2\tan^2\nu}, \tag{A4}$$

where ν' is the angle between the extraordinary ray and the optical axis, related to ν by

$$\tan\nu'=\frac{n_o^2}{n_e^2}\tan\nu. \tag{A5}$$

When the light beam is incident normally (i.e., the incident angle is 0) on the uniaxial crystal interface, the wave normal directions of the o-wave and e-wave inside the crystal are identical and both are perpendicular to the crystal surface. Since the ray direction of the o-ray coincides with its wave normal, the o-ray is perpendicular to the crystal surface. For the e-ray, the angle α between its ray direction and the e-wave normal can be calculated using Eq. (A4). In this case, the e-ray deviates from the optical axis relative to its wave normal. Given that the e-wave normal shares the same direction as the o-wave normal, the angle α represents the angle between the e-ray and the o-ray. Consequently, the shear distance generated by the uniaxial crystal can be derived as

$$\delta=\frac{d}{2}\tan\alpha, \tag{A6}$$

where d is the thickness of the crystal.

Appendix B: Effect of transmission distance on differential interference

In this section, the evolution of differential interference effects with propagation distance is analyzed, with specific comparison made between the results at $z=0\,\mathrm{mm}$ and $z=400\,\mathrm{mm}$. Two cases are examined: Case 1 is sensitive to the imaginary part of the initial displacement, and Case 2 to its real part.

Case 1 is discussed first. The corresponding interference patterns at $z=0\,\mathrm{mm}$ are shown in Figs. A1(a_i)–(h_i) for $i=2,3$. A comparison with the results at $z=400\,\mathrm{mm}$ in Figs. A2(a_i)–(h_i) reveals that no significant centroid shift is observed in subplots (d_i) and (h_i) at $z=0\,\mathrm{mm}$. Upon propagation, the field evolves according to the transfer function in the angular spectrum representation. When the propagation distance is increased to $z=400\,\mathrm{mm}$, different spatial frequency components accumulate distinct phase delays, leading to a significant evolution in the relative phase difference between the two interfering components compared to that at $z=0\,\mathrm{mm}$. This phase evolution transforms the differential interference pattern to evolve from Figs. A1(d_i) and (h_i) to Figs. A2(d_i) and (h_i), and the corresponding phase

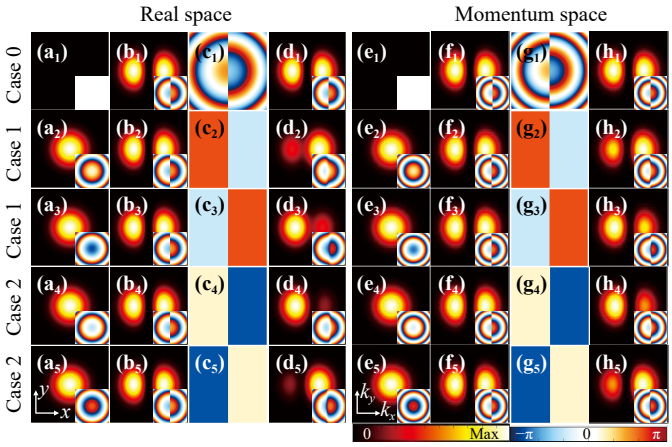

Fig. A1 Simulated beam interference patterns in r-space [panels $(\mathbf{a_i}-\mathbf{d_i})$] and k-space [panels $(\mathbf{e_i}-\mathbf{h_i})$] at $z = 0\,\mathrm{mm}$. (a_i) and (e_i) Intensity distribution of the Gaussian field component. (b_i) and (f_i) Intensity distribution of the first-order partial derivative of the Gaussian field with respect to x. (c_i) and (g_i) Phase difference between the Gaussian field and the interfering field. (d_i) and (h_i) Intensity distribution of the resulting interference field. Each panel includes an inset showing the corresponding phase distribution. Subgraphs (a_i) to (d_i) share the same coordinate system (x, y), while subgraphs (e_i) to (h_i) share the same coordinate system (k_x, k_y). The subscript $i = 1$ to 5 corresponds to the following (α, β) angle pairs: $(0°, 0°)$, $(2°, 0°)$, $(-2°, 0°)$, $(0°, 2°)$, and $(0°, -2°)$, respectively.

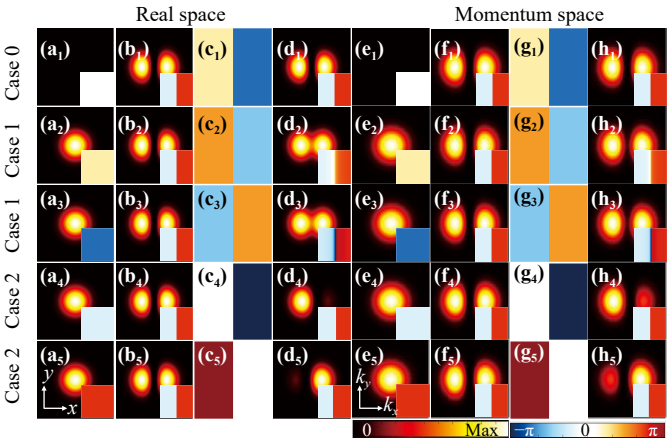

Fig. A2 Simulated beam interference patterns in r-space [panels $(\mathbf{a_i}-\mathbf{d_i})$] and k-space [panels $(\mathbf{e_i}-\mathbf{h_i})$] at $z = 400\,\mathrm{mm}$. (a_i) and (e_i) Intensity distribution of the Gaussian field component. (b_i) and (f_i) Intensity distribution of the first-order partial derivative of the Gaussian field with respect to x. (c_i) and (g_i) Phase difference between the Gaussian field and the interfering field. (d_i) and (h_i) Intensity distribution of the resulting interference field. Each panel includes an inset showing the corresponding phase distribution. Subgraphs (a_i) to (d_i) share the same coordinate system (x, y), while subgraphs (e_i) to (h_i) share the same coordinate system (k_x, k_y). The subscript $i = 1$ to 5 corresponds to the following (α, β) angle pairs: $(0°, 0°)$, $(2°, 0°)$, $(-2°, 0°)$, $(0°, 2°)$, and $(0°, -2°)$, respectively.

difference map changes from Figs. A1(c_i) and (g_i) to Figs. A2(c_i) and (g_i). By adjusting the parameter α, the relative weight of the two field components is modified, whereby the interference contrast is controlled. It should be noted that the spatial positions of the interference fringes are determined solely by the wavefront geometry and remain invariant with respect to α, while only the fringe visibility is modulated.

The response of Case 2 is further analyzed in both r-space and k-space. As shown in Figs. A1(a_i)–(h_i) for $i = 4, 5$, a pronounced centroid shift is already visible in subplots (d_i) and (h_i) at $z = 0\,\mathrm{mm}$. This is consistent with a discontinuous jump from 0 to π in the phase difference map at the origin $(x = 0, y = 0)$, reflecting the imposed spatial phase discontinuity. When the propagation distance is increased to $z = 400\,\mathrm{mm}$, the transfer function further modulates the spectral components, resulting in an enhanced contrast of the differential signal. Consequently, the interference pattern evolves from Figs. A1(d_i) and (h_i) to Figs. A2(d_i) and (h_i), and the phase difference map changes from Figs. A1(c_i) and (g_i) to Figs. A2(c_i) and (g_i). By adjusting the parameter β, the relative amplitude of the two field components is controlled, whereby the interference contrast is tuned without affecting the fringe positions. A significant lateral shift is observed for the central dark fringe.

References

1. G. Nomarski, Differential microinterferometer with polarized waves, *J. Phys. Radium* 16, 9S (1955)
2. W. Lang, Nomarski differential Interference Contrast Microscopy, *Zeiss Information* 70, 114 (1968)
3. D. J. Goldberg and D. W. Burmeister, Stages in axon formation: observations of growth of Aplysia axons in culture using video-enhanced contrast-differential interference contrast microscopy, *J. Cell Biol.* 103(5), 1921 (1986)
4. J. Rogers and C. Keevil, Immunogold and fluorescein immunolabelling of Legionella pneumophila within an aquatic biofilm visualized by using episcopic differential interference contrast microscopy, *Appl. Environ. Microbiol.* 58(7), 2326 (1992)
5. S. H. Kang, S. Lee, and E. S. Yeung, Direct observation of single native dna molecules in a microchannel by differential interference contrast microscopy, *Anal. Chem.* 76(15), 4459 (2004)
6. A. Tamada and M. Igarashi, Revealing chiral cell motility by 3D Riesz transform-differential interference contrast microscopy and computational kinematic analysis, *Nat. Commun.* 8(1), 2194 (2017)
7. X. Wang, H. Wang, J. Wang, X. Liu, H. Hao, Y. S. Tan, Y. Zhang, H. Zhang, X. Ding, W. Zhao, Y. Wang, Z. Lu, J. Liu, J. K. W. Yang, J. Tan, H. Li, C. W. Qiu, G. Hu, and X. Ding, Single-shot isotropic differential interference contrast microscopy, *Nat. Commun.* 14(1),

2063 (2023)
8. D. San Martín, Y. Palizdar, R. Cochrane, R. Brydson, and A. Scott, Application of Nomarski differential interference contrast microscopy to highlight the prior austenite grain boundaries revealed by thermal etching, *Mater. Charact.* 61(5), 584 (2010)
9. L. Xiao, J. W. Ha, L. Wei, G. Wang, and N. Fang, Determining the full three-dimensional orientation of single anisotropic nanoparticles by differential interference contrast microscopy, *Angew. Chem. Int. Ed.* 51(31), 7734 (2012)
10. F. Araiedh, F. Ducos, A. Houas, and N. Chaoui, Photodegradation mode of stearic acid crystal on heterogeneous anatase/amorphous titania films observed by differential interference contrast microscopy, *Appl. Catal. B* 187, 350 (2016)
11. Z. Q. Wen, G. Torraca, P. Masatani, C. Sloey, and J. Phillips, Nondestructive detection of glass vial inner surface morphology with differential interference contrast microscopy, *J. Pharm. Sci.* 101(4), 1378 (2012)
12. Z. Zeng, C. Zhang, S. Du, and X. Chen, Quantitative surface topography of martensitic microstructure by differential interference contrast microscopy, *J. Mech. Phys. Solids* 124, 102 (2019)
13. Y. Shou, J. Liu, and H. Luo, When optical microscopy meets all-optical analog computing: A brief review, *Front. Phys. (Beijing)* 18(4), 42601 (2023)
14. J. Deng, L. Deng, Z. Guan, J. Tao, G. Li, Z. Li, Z. Li, S. Yu, and G. Zheng, Multiplexed anticounterfeiting meta-image displays with single-sized nanostructures, *Nano Lett.* 20(3), 1830 (2020)
15. X. Bi, X. Guo, X. Wu, X. Fan, B. Wei, D. Wen, S. Liu, J. Zhao, and P. Li, Wideband optical edge detection based on dielectric metasurface, *Appl. Phys. Lett.* 123(6), 061702 (2023)
16. D. Xu, W. Xu, Q. Yang, W. Zhang, S. Wen, and H. Luo, All-optical object identification and three-dimensional reconstruction based on optical computing metasurface, *Opto-Electron. Adv.* 6, 230120 (2023)
17. Q. Li, M. Liang, S. Liu, J. Liu, S. Chen, S. Wen, and H. Luo, Phase reconstruction via metasurface-integrated quantum analog operation, *Opto-Electron. Adv.* 8(4), 240239 (2025)
18. J. Liu and H. Luo, Metasurface differential optics: from classical to quantum, *Rev. Opto-Electron.* 1, 260001 2026
19. C. Preza, D. L. Snyder, and J. A. Conchello, Theoretical development and experimental evaluation of imaging models for differential-interference-contrast microscopy, *J. Opt. Soc. Am. A* 16(9), 2185 (1999)
20. M. R. Arnison, K. G. Larkin, C. J. R. Sheppard, N. I. Smith, and C. J. Cogswell, Linear phase imaging using differential interference contrast microscopy, *J. Microsc.* 214(1), 7 (2004)
21. S. S. Kou, L. Waller, G. Barbastathis, and C. J. Sheppard, Transport-of-intensity approach to differential interference contrast (TI-DIC) microscopy for quantitative phase imaging, *Opt. Lett.* 35(3), 447 (2010)
22. S. Gao, J. Xiong, A. K. Yetisen, F. Salazar-Bloise, A. W. Koch, X. Yang, and S. Wang, Vector differential interference contrast microscopy based on a 3-in-1 phase mask through a dynamic diffractive optical element, *ACS Photonics* 11(1), 276 (2024)
23. H. Yang, W. Xie, H. Chen, M. Xie, J. Tang, H. Zheng, Y. Zhong, J. Yu, Z. Chen, and W. Zhu, Spin–orbit optical broadband achromatic spatial differentiation imaging, *Optica* 11(7), 1008 (2024)
24. L. T. Su, C. Peng, Z. H. Guo, C. T. Xu, and W. Hu, Multi-order optical differentiator integrated with an omnidirectionally selective subtracter, *Appl. Phys. Lett.* 127(9), 091104 (2025)
25. J. Chen, Y. Xu, X. Lv, X. Lai, and S. Zeng, Super-resolution differential interference contrast microscopy by structured illumination, *Opt. Express* 21(1), 112 (2013)
26. N. W. M. Ritchie, J. G. Story, and R. G. Hulet, Realization of a measurement of a "weak value", *Phys. Rev. Lett.* 66(9), 1107 (1991)
27. H. Luo, X. Zhou, W. Shu, S. Wen, and D. Fan, Enhanced and switchable spin Hall effect of light near the Brewster angle on reflection, *Phys. Rev. A* 84(4), 043806 (2011)
28. L. Zhang, A. Datta, and I. A. Walmsley, Precision metrology using weak measurements, *Phys. Rev. Lett.* 114(21), 210801 (2015)
29. S. Chen, X. Zhou, C. Mi, Z. Liu, H. Luo, and S. Wen, Dielectric metasurfaces for quantum weak measurements, *Appl. Phys. Lett.* 110(16), 161115 (2017)
30. X. Lu, L. Xu, L. Luo, Z. Li, T. Chang, D. Wei, and H. L. Cui, Weak value amplified precision terahertz spectroscopic detection of solid and liquid glucose samples, *ACS Photonics* 10(9), 3149 (2023)
31. Y. Wang, J. Zhu, Y. Jiang, Y. Liu, A. Wang, L. Ye, J. Wu, R. Ge, F. Gao, and Z. Zhang, Fast-response and stable weak measurement system for protein–antibody specific detection, *Sens. Actuators B* 426, 136828 (2025)
32. J. Zhu, L. Ye, Y. Wang, Y. Liu, Y. Jiang, A. Wang, J. Wu, and Z. Zhang, Weak value and measurement in precision sensing, *Appl. Phys. Rev.* 12(2), 021315 (2025)
33. Y. Wang, S. Yang, Q. Zhang, Y. Chen, X. Hu, H. Zhang, and Z. Zhang, Fast-response and stable weak measurement system for protein–antibody specific detection, *APL Photon.* 8(12), 126102 (2023)
34. L. Xu, L. Luo, H. Wu, Z. Luo, Z. Zhang, H. Shi, T. Chang, P. Wu, C. Du, and H. L. Cui, Measurement of chiral molecular parameters based on a combination of surface plasmon resonance and weak value amplification, *ACS Sens.* 5(8), 2398 (2020)
35. Y. Wang, J. Zhu, J. Wu, R. Ge, F. Gao, and Z. Zhang, High-precision weak measurement sensing with adaptability in sensitivity, *Appl. Phys. Lett.* 124(13), 131102 (2024)
36. M. Onoda, S. Murakami, and N. Nagaosa, Hall effect of light, *Phys. Rev. Lett.* 93(8), 083901 (2004)
37. K. Y. Bliokh and Y. P. Bliokh, Conservation of angular momentum, transverse shift, and spin Hall effect in reflection and refraction of an electromagnetic wave packet, *Phys. Rev. Lett.* 96(7), 073903 (2006)
38. X. Yin, Z. Ye, J. Rho, Y. Wang, and X. Zhang, Photonic spin Hall effect at metasurfaces, *Science* 339(6126), 1405 (2013)
39. X. Ling, X. Zhou, K. Huang, Y. Liu, C. W. Qiu, H. Luo, and S. Wen, Recent advances in the spin Hall

effect of light, *Rep. Prog. Phys.* 80(6), 066401 (2017)
40. Z. Li, W. Liu, H. Cheng, S. Chen, and J. Tian, Manipulation of the photonic spin Hall effect with high efficiency in gold-nanorod-based metasurfaces, *Adv. Opt. Mater.* 5(20), 1700413 (2017)
41. M. Neugebauer, S. Nechayev, M. Vorndran, G. Leuchs, and P. Banzer, Weak measurement enhanced spin Hall effect of light for particle displacement sensing, *Nano Lett.* 19(1), 422 (2019)
42. X. Ling, Z. Zhang, Z. Dai, Z. Wang, H. Luo, and L. Zhou, Photonic spin-Hall effect at generic interfaces, *Laser Photonics Rev.* 17(4), 2200783 (2023)
43. Y. Kim, X. Li, P. Tang, G. Li, and J. Rho, Spin-dependent phenomena of meta-optics, *ACS Photonics* 12(1), 16 (2025)
44. Q. Yang, Y. Shou, S. Chen, S. Wen, and H. Luo, Quantum weak value enabled quantitative phase imaging, *Laser Photonics Rev.* 19(3), 2400092 (2025)
45. L. Tang, Q. Yang, J. Liu, Y. Gao, Y. Shou, D. Zheng, S. Chen, and H. Luo, Observation of the spin Hall effect of light via differential interference, *Phys. Rev. Appl.* 23(6), 064037 (2025)
46. Y. Aharonov, D. Z. Albert, and L. Vaidman, How the result of a measurement of a component of the spin of a spin-1/2 particle can turn out to be 100, *Phys. Rev. Lett.* 60(14), 1351 (1988)
47. I. M. Duck, P. M. Stevenson, and E. C. G. Sudarshan, The sense in which a "weak measurement" of a spin-½ particle's spin component yields a value 100, *Phys. Rev. D* 40(6), 2112 (1989)
48. K. Y. Bliokh, F. J. Rodríguez-Fortuño, F. Nori, and A. V. Zayats, Spin–orbit interactions of light, *Nat. Photonics* 9(12), 796 (2015)
49. S. Wu and Y. Li, Weak measurements beyond the Aharonov–Albert–Vaidman formalism, *Phys. Rev. A* 83(5), 052106 (2011)
50. J. Dressel and A. N. Jordan, Weak values are universal in von Neumann measurements, *Phys. Rev. Lett.* 109(23), 230402 (2012)
51. A. Di Lorenzo, Full counting statistics of weak-value measurement, *Phys. Rev. A* 85(3), 032106 (2012)
52. N. Ghosh and K. Bhattacharya, Polarization phase-shifting interferometric technique for complete evaluation of birefringence, *Appl. Opt.* 50(15), 2179 (2011)
53. B. A. Palmer, G. R. Edwards-Gau, A. Morte-Ródenas, B. M. Kariuki, G. K. Lim, K. D. M. Harris, I. P. Dolbnya, and S. P. Collins, X-ray birefringence: A new strategy for determining molecular orientation in materials, *J. Phys. Chem. Lett.* 3(21), 3216 (2012)
54. E. Mohammadi, K. Tsakmakidis, A. N. Askarpour, P. Dehkhoda, A. Tavakoli, and H. Altug, Nanophotonic platforms for enhanced chiral sensing, *ACS Photonics* 5(7), 2669 (2018)
55. A. Tudi, S. Han, Z. Yang, and S. Pan, Potential optical functional crystals with large birefringence: Recent advances and future prospects, *Coord. Chem. Rev.* 459, 214380 (2022)
56. V. Jaberian Hamedan, A. Adam, C. Blair, L. Ju, and C. Zhao, Precision mapping of a silicon test mass birefringence, *Appl. Phys. Lett.* 122(6), 064101 (2023)
57. S. Chen, X. Zhou, C. Mi, H. Luo, and S. Wen, Modified weak measurements for the detection of the photonic spin Hall effect, *Phys. Rev. A* 91(6), 062105 (2015)
58. A. Ghosh and P. Fischer, Chiral molecules split light: Reflection and refraction in a chiral liquid, *Phys. Rev. Lett.* 97(17), 173002 (2006)
59. R. Wang, J. Zhou, K. Zeng, S. Chen, X. Ling, W. Shu, H. Luo, and S. Wen, Ultrasensitive and real-time detection of chemical reaction rate based on the photonic spin Hall effect, *APL Photonics* 5(1), 016105 (2020)
60. M. Born and E. Wolf, Principles of Optics: Electromagnetic Theory of Propagation, Interference and Diffraction of Light, Elsevier, 2013